Optical Frequency Combs in External Cavity SiN Hybrid Lasers

Optical Frequency Combs in External Cavity SiN Hybrid Lasers

Cristina Rimoldi, *Member, IEEE*, Lorenzo L. Columbo, and Mariangela Gioannini, *Member, IEEE*

***Abstract*—We analyze the emergence of optical frequency combs in a III-V SiN hybrid laser. Our model accounts for the narrow band effective mirror reflectivity and allows to simulate laser dynamics as a function of the bias current and the detuning of the lasing frequency with respect to the effective reflectivity peak. The physical mechanisms triggering multimode dynamics are analyzed in detail, with a focus on the generation of frequency combs, which are characterized in terms of bandwidth, line separation, phase and amplitude noise.**

***Index Terms*—Hybrid integrated lasers, optical frequency combs, semiconductor lasers, silicon photonics.**

I. Introduction

OPTICAL frequency combs currently identify one of the most rapidly developing areas in photonic research, due to their captivating potential for a wide variety of applications, ranging from molecular spectroscopy and Laser Imaging, Detection, And Ranging (LIDAR) to broadband free-space optical communication and wavelength-division multiplexed (WDM) systems in datacom technologies [1]. In this context, Silicon Photonic integration allows for CMOS-compatible, low-cost devices characterized by reduced system size, weight, and power consumption, which makes them very suitable for out-of-the-lab applicability. In recent years, the generation of on-chip Optical Frequency Combs (OFCs) has seen a rapid technological growth [1], on the other hand, the integrated devices generating OFCs usually need to be driven by bulk electronic and optical equipment for coherent injection. Here, integrated laser sources offer a potential compact solution for the spontaneous generation of OFCs, as experimentally demonstrated in recent years [2], [3], [4], [5]. While these results show promise for a full integration of OFC generation devices on Silicon Photonic (SiPh) circuits, they currently require a more detailed theoretical and numerical study in order to address the physical mechanisms leading to their generation as well as their stability requirements. In literature, integrated lasers have been extensively studied for Continuous Wave (CW) applications in the context of high-speed optical transceivers in CMOS-compatible technology, where narrow optical linewidth sources are typically required [6], but only a few works have focused on the multimode dynamics occurring in different operative regimes [2], [3]. Additionally, OFC generation in hybrid integrated lasers with a reversely biased saturable absorber section, providing passive mode-locking, have been demonstrated [7]. While this allows to achieve large comb bandwidth, such configurations lack stability, especially at low repetition rates, due to pulse-to-pulse spontaneous emission amplification [8]. To overcome this problem, SiPh circuits including coupled microrings, providing spectral filtering via Vernier effect, can be considered. In this paper, we provide a suitable theoretical and numerical framework for the study of CW and multimode dynamics in a hybrid integrated laser (see also Fig. 1), where such a solution is adopted and OFCs can be self-generated as a result of the sole Direct Current (DC) bias of the gain region. Recent contributions in similar platforms [2] have justified OFC occurrence with the almost symmetric distribution of longitudinal modes around the peak of the effective reflection coefficient provided by the SiPh integrated circuit that acts as an external cavity mirror. Here, we show that OFCs can also appear when the laser modes are asymmetrically detuned with respect to the reflectivity peak and arise from the combined effect of Four-Wave Mixing (FWM), undamped relaxation oscillations, and a non-null Henry factor. In comparison with Kerr OFCs in passive devices, the proposed structure relaxes the requirements for very high-Q ring resonators [6]. Our simulated

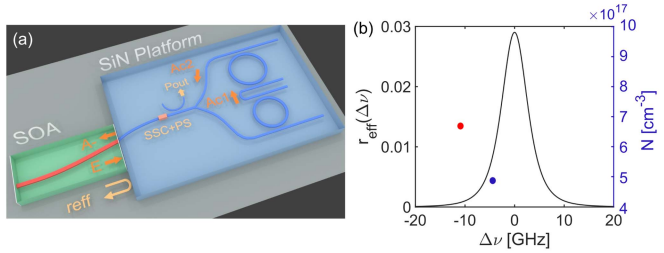

Fig. 1. (a) Hybrid integrated laser considered throughout the study. SOA: Semiconductor optical amplifier; SSC: Spot size converter; PS: Phase section; P_{out}: Output power. E, A_{c1}, A_{c2}, and A^- are the electric fields in (1)–(4). (b) Example of the resulting effective reflectivity of the SiN circuit, with an FWHM = 6 GHz (in black,left y-axis). We also indicate (right y-axis) the only two solutions (ω_s, N_s) of the oscillation condition in the ± 20 GHz range with the blue and red points. In this example the blue solution at -4.38 GHz is the lasing mode with the lowest threshold. It has been detuned with respect to 0 GHz by applying $\Delta\phi = 6$ rad to the PS.

Manuscript received 13 February 2024; accepted 14 February 2024. Date of publication 20 February 2024; date of current version 1 March 2024. This work was supported in part by the European Union under the Italian National Recovery and Resilience Plan (PNRR) of NextGenerationEU, partnership on "Telecommunications of the Future" (PE00000001 - program "RESTART"). The work of Cristina Rimoldi was supported by the Programma Operativo Nazionale (PON) Ricerca e Innovazione of the Italian Ministry of University and Research under Research Contract [32- I-13427-1] (DM 1062/2021). *(Corresponding author: Cristina Rimoldi.)*

The authors are with the Dipartimento di Elettronica e Telecomunicazioni, Politecnico di Torino, 10129 Torino, Italy (e-mail: cristina.rimoldi@polito.it; lorenzo.columbo@polito.it; mariangela.gioannini@polito.it).

Digital Object Identifier 10.1109/JPHOT.2024.3367542

OFCs display both amplitude and frequency modulation, and present −20 dB bandwidths up to 100 GHz and optical line spacing between 5.5 GHz and 10 GHz.

The paper is structured as follows. In Section II, we describe the laser that we aim to model and provide the theoretical framework for the study of the overall laser stability. In Section III, we demonstrate through our numerical results the physical mechanisms leading to the instability of single mode solutions. In Section IV, we illustrate the more accurate Time Domain Traveling Wave model employed to characterize OFC solutions, differing from the model in Section II mainly by accounting for the electric field and carrier density spatial distribution in the propagation direction in the RSOA. The simulated OFCs are then characterized in terms of phase and amplitude noise, bandwidth, and line separation.

II. Device and Modeling

The device we aim to analyze is illustrated in Fig. 1(a): it comprises a III-V Multiple Quantum Well High reflection/Antireflection (HR/AR) Reflective Semiconductor Optical Amplifier (RSOA) that is edge-coupled to a SiN circuit, which includes two coupled rings. The ring configuration provides an effective narrow band reflectivity $|r_{eff}|^2$ to the right of the RSOA due to Vernier effect, with Full Width at Half Maximum (FWHM) of a few GHz [9]. We sketch an example of the resulting effective reflectivity in Fig. 1(b). The laser power output is collected at the output coupler, placed before the splitter. Further, a phase section is included in the SiPh platform in order to allow detuning of the lasing frequency with respect to the effective reflectivity peak. Typical device parameters considered throughout the text are about 1 mm for the RSOA length and 100 μm for the ring radii. The length of the bus waveguide that connects the SSC to the ring input is about 1.5 mm.

In order to address the cause of CW instability in this laser, we model this device via a set of delayed algebraic rate equations, based on the approach reported in [10]. Our model, developed in the neighborhood of the CW solutions, allows to properly account for longitudinal mode competition, as well as for the narrow band of the effective reflectivity. Such a model has been previously employed to characterize the laser stability and address feedback resilience [9], [11] to spurious back reflections. In this paper, we focus on its use to address the onset of multimode dynamics and, specifically, the generation of optical frequency combs.

The model is the following

$$E(t) = \frac{e^{i(\omega_s-\omega_0)\tau_{in}} \exp f(\omega_s, N_s)}{r_{eff}(\omega_s)} A^-(t-\tau_{in}) + F(t) \tag{1}$$

$$\frac{\mathrm{d}A_{c1}(t)}{\mathrm{d}t} = \gamma_{c1} t_{tr} E(t-\tau_{in,SiN}/2) e^{-i\frac{\Delta\phi}{2}} - \gamma_{t1} A_{c1}(t) \tag{2}$$

$$\frac{\mathrm{d}A_{c2}(t)}{\mathrm{d}t} = \gamma_{c2} A_{c1}(t) - \gamma_{t2} A_{c2}(t) \tag{3}$$

$$\frac{\mathrm{d}N(t)}{\mathrm{d}t} = \frac{\eta_i I}{qV} - \frac{N(t)}{\tau_N} - v_g g_N \ln\left(\frac{N(t)}{N_0}\right) \sigma \frac{|E(t)|^2}{V} \tag{4}$$

with

$$A^-(t-\tau_{in}) = t_{tr} e^{-i\frac{\Delta\phi}{2}} A_{c2}(t-\tau_{in}-\tau_{in,SiN}/2)$$

$$f(\omega_s, N_s) = \frac{1}{\tau_{in}} \int_{t-\tau_{in}}^{t} L\left(1 + i\alpha\frac{\omega_s}{\omega_0}\right) g_N \ln\left(\frac{N(\bar{t})}{N_s}\right) \mathrm{d}\bar{t}$$

and effective reflectivity

$$r_{eff}(\omega) = \frac{\gamma_{c1}\gamma_{c2} t_{tr}^2}{(\gamma_{t1} + i\Delta\omega)(\gamma_{t2} + i\Delta\omega)} e^{-i\Delta\phi} e^{-i\Delta\omega\tau_{in,SiN}}, \tag{5}$$

where $E(t)$ is the slowly varying envelope of the electric field exiting the RSOA through the AR-coated facet, $A_{c1}(t)$ is the field at the drop port of ring 1, $A_{c2}(t)$ is the field after propagation in the second ring (see Fig. 1(a)), and $N(t)$ is the carrier density in the RSOA. Eq. (1) accounts for the dynamics of the electric field within the RSOA. Here, ω_s is the angular frequency of the CW solution and $\omega_0 = 2\pi c/\lambda_0 \approx 1.45 \times 10^{15}$ rad/s, with $\lambda_0 = 1.31$ μm, is the reference angular frequency, which matches the effective reflectivity peak ($\Delta\omega = \omega - \omega_0$). The RSOA cavity roundtrip time is τ_{in} and $\tau_{in,SiN}$ is the time delay related to the bus waveguide sections in the SiPh circuit. The linewidth enhancement factor is α and $\Delta\phi$ is the phase shift due to the phase control section in the circuit. The coefficients of the effective reflectivity, given in (5), are $\gamma_{c1,2}$, i.e., the coupling rates of the electric field into ring 1,2 from the bus waveguide and $\gamma_{t1,2}$, i.e., the rates at which the electric field is lost (either because of coupling out of the bus waveguide or because of waveguide losses) [9], [12]. Eqs. (2)–(3) are each valid around one ring resonance, which is approximated with a Lorentzian function [12]. All other ring resonances can be neglected because they are strongly attenuated by Vernier effect. The transmission coefficient $t_{tr} = t_{SSC}\sqrt{1-T_{c,out}}$ accounts for the Spot Size Converter transmission at the entrance of the SiPh circuit (t_{SSC}, accounting for an insertion loss of 2 dB) and for the output coupler power transmission coefficient, $T_{c,out} = 73\%$ (chosen to optimize wall-plug efficiency [13]). Eq. (4) describes the dynamics of the carrier density in the RSOA. Here, η_i is the internal quantum efficiency, I is the bias current, q is the electron charge, V is the volume of the active region, and N_0 is the carrier density at transparency. Further, τ_N is the carrier lifetime, v_g is the group velocity, and g_N is the modal gain coefficient in the RSOA. Finally, σ is a coefficient accounting for the spatial average of the optical power along the RSOA. For additional considerations and more details on variable normalizations, values of the simulation and structure parameters, we direct the reader to [9].

III. Simulation of Optical Frequency Combs

The laser cavity modes can be calculated as the single mode solutions of the laser oscillation condition, imposing that the product of left and right reflectivity at the AR-coated facet of the RSOA equals 1. Such solutions, illustrated in Fig. 1(b) with the red and blue points, correspond to different frequencies ($\Delta\nu_s = \Delta\omega_s/2\pi$) and associated carrier density (N_s, right y-axis). The solution with the lowest N_s (in blue) will be the lasing one in single mode emission. The asymmetry of the solutions with

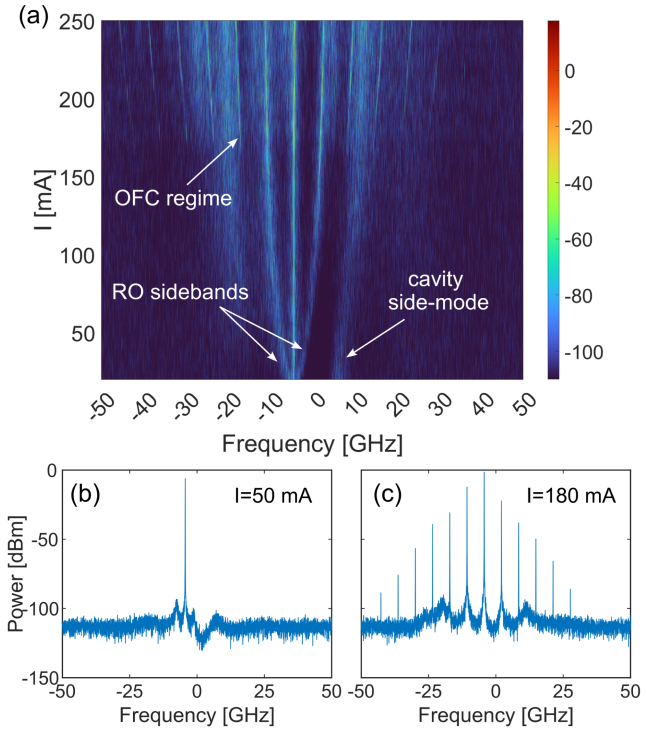

Fig. 2. Optical spectra for the detuning condition illustrated in Fig. 1(b) and increasing current.

respect to 0 GHz is due to the non-null α parameter, set in this case to $\alpha = 3$.

In Fig. 2(a), we illustrate the typical process giving rise to CW instability by showing a map of the optical spectra at increasing current above threshold. In this example, the lasing mode is detuned with respect to the peak of $|r_{eff}|^2$ by $\Delta\nu_s = \Delta\omega_s/2\pi = -4.38$ GHz, as indicated in Fig. 1(b). In this configuration, the laser becomes unstable for a bias current $I \approx 170$ mA. In single mode emission (low currents), the laser optical spectra present, aside from the main spectral peak, relaxation oscillation sidebands, as expected; see e.g., Fig. 2(b), where we report the optical spectrum at 50 mA. Further, we can observe the additional emergence of cavity side-modes, which are the other laser longitudinal modes at the wavelengths that guarantee a 2π phase shift after a roundtrip with carrier density in the RSOA clamped at the threshold of the lasing mode [14]. Note that these cavity side-modes are different from the solutions of the oscillation condition (reported with a red point in Fig. 1(b)) because of the non-null α factor of the SOA [9]. From Fig. 2, we can observe how the gradual undamping of relaxation oscillations (ROs) gives rise to CW instability. In particular, α allows for the efficient conversion of phase noise into intensity noise, which then enhances again the phase noise, eventually leading to the undamping of relaxation oscillations in cases where no opposite stabilization mechanisms, such as detuned loading [6], come into play. In this configuration, if the frequency of RO is comparable with the frequency separation between two solutions ω_s (reported in Fig. 1(b)), then such a resonance favors the occurrence of multimode regimes. This is indeed what happens in Fig. 2, where the frequency separation between the two solutions ω_s (displayed in Fig. 1(b)) is about 6.5 GHz and relaxation oscillations at a bias current of 170 mA have a very similar frequency. Finally, FWM is the mechanism that ultimately provides mode proliferation through parametric gain and phase locking of the comb lines, resulting in the OFC. We highlight that other multimode regimes (i.e., quasi-turbulent or chaotic) can also occur (i) for much higher current values where the laser trajectory excursion in the phase space can be even larger, potentially experiencing the effect of other attractors, as well as (ii) for larger detuning, when the CW solutions potentially leading to the aforementioned resonance effect are beyond FWM locking range, because of dispersion. Finally, we highlight that comb generation does not take place if the lasing frequency is not detuned with respect to the effective reflectivity peak [9].

IV. Optical Frequency Comb Characterization

A. Time Domain Traveling Wave Modeling

Now that we have addressed the mechanism giving rise to OFC formation, we want to characterize the resulting comb in terms of phase and intensity noise of the single lines. The model in (1)–(4) is ideal for addressing the causes of CW instability, due to the short simulation time and the possibility to conduct linear stability analyses [9]. However, since it is valid only in a frequency range around the CW solution, it could become less accurate when the CW solution becomes unstable, occupying a wider bandwidth. While this is not the case e.g., for the simulations illustrated in Fig. 2, we expect that well into the comb regimes (e.g. at a current $I = 300$ mA) the simulation results may become less precise. For this reason, in the characterization of OFCs we adopt the following Time Domain Traveling Wave (TDTW) model [15], [16].

$$\frac{\partial E^{\pm}(z,t)}{\partial t} \pm v_g \frac{\partial E^{\pm}(z,t)}{\partial z} = -\frac{E^{\pm}(z,t)}{2\tau_p} + \frac{v_g g_N}{2}(1+i\alpha)\log\left(\frac{N(z,t)}{N_0}\right)E^{\pm}(z,t) + F(z,t) \tag{6}$$

$$\frac{\mathrm{d}A_{c1}(t)}{\mathrm{d}t} = \gamma_{c1} t_{tr} E^{+}(L, t-\tau_{in,SiN}/2) e^{-i\frac{\Delta\phi}{2}} - \gamma_{t1} A_{c1}(t) \tag{7}$$

$$\frac{\mathrm{d}A_{c2}(t)}{\mathrm{d}t} = \gamma_{c2} A_{c1}(t) - \gamma_{t2} A_{c2}(t) \tag{8}$$

$$\frac{\partial N(z,t)}{\partial t} = \frac{\eta_i I}{qV} - \frac{N(z,t)}{\tau_N} - \frac{\epsilon v_g g_N}{2\Gamma\hbar\omega_0}\log\left(\frac{N(z,t)}{N_0}\right)|E_{tot}|^2 \tag{9}$$

with boundary condition

$$E^{-}(L,t) = A_{c2}(t)$$

where $|E_{tot}|^2 = |E^{+}|^2 + |E^{-}|^2$ is proportional to the optical power in the section $\mathrm{d}z$ of the RSOA and it is given by the sum of the intensities of the (slowly varying) forward $E^{+}(z,t)$ and

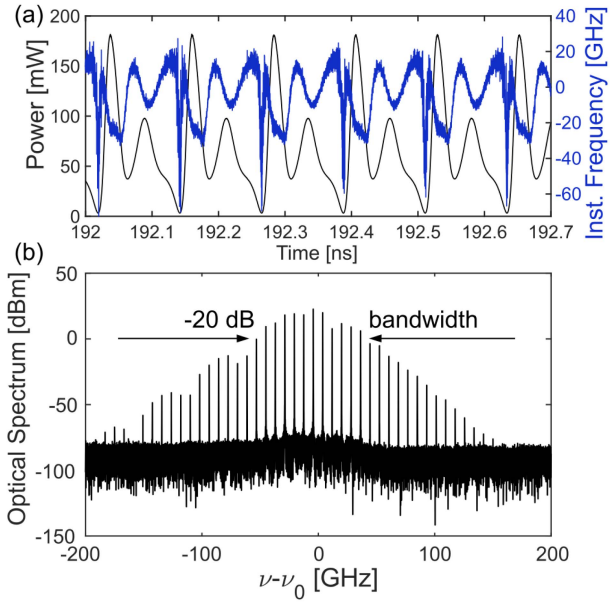

Fig. 3. (a) Amplitude and frequency modulation in an OFC regime for $|r_{eff}|^2$ FWHM = 6 GHz and (b) resulting optical spectrum. This result is obtained with the TDTW model.

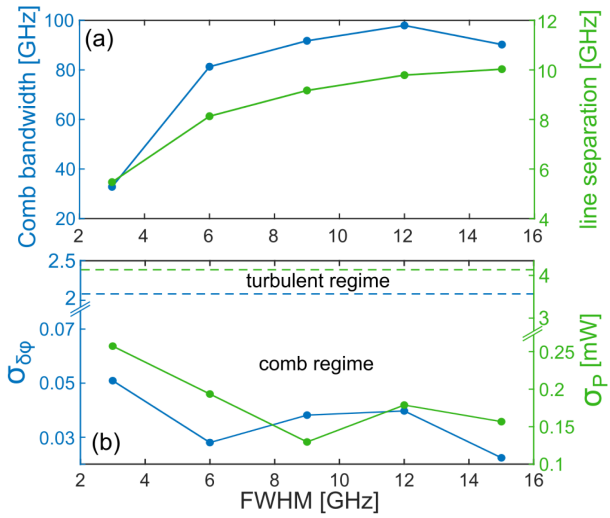

Fig. 4. (a) OFC −20 dB bandwidth (in blue) and spectral line separation (in green) as a function of the effective reflectivity FWHM. (b) Phase (in blue) and amplitude (in green) noise quantifiers as a function of the FWHM. The upper part of the plot features a different scale in order to display the quantifier values for turbulent regimes (dashed lines).

backward $E^-(z,t)$ propagating field. The confinement factor is Γ. The main difference between the TDTW model in (6)–(9) and the delayed algebraic equation model in (1)–(4) is the fact that, here, we are fully accounting for the spatial distribution of the electric field and carrier density in the RSOA. This also implies a spatial dependence in the term $F(z,t)$ accounting for spontaneous emission. Eq. (6)–(9) are numerically solved through split-step method. Note that while, in (1)–(4), $|E(t)|^2$ is normalized to be the power of the electric field [10], here $|E_{tot}|^2$ is normalized so that $\epsilon|E_{tot}|^2/2\hbar\omega_0$ is the photon density (with $\epsilon = \epsilon_0 n^2$ being the medium permittivity and n being the background refractive index).

B. Comb Features

In Fig. 3, we show an example of an OFC regime, obtained by integrating (6)–(9), at $|r_{eff}|^2$ FWHM=6 GHz, for a bias current $I = 300$ mA and a detuning condition similar to the one illustrated in Fig. 1(b). Here, we can observe the presence of a strong modulation both in power (i.e., Amplitude Modulation, AM, in black) and instantaneous frequency (i.e., Frequency Modulation, FM, in blue). The resulting OFC is shown in Fig. 3(b) where we observe a −20 dB bandwidth of about 80 GHz.

We are interested in studying the impact of the SiPh reflector bandwidth on the formation of OFCs. For this reason, we have performed several simulations of hybrid lasers with different $|r_{eff}|^2$ FWHMs and we have analyzed the results for a fixed RSOA bias current of 300 mA and by sweeping the phase $\Delta\phi$. When the comb regime was found, we have searched for the detuning $\Delta\nu$ (and consequent PS $\Delta\phi$) that maximizes the comb bandwidth. In Fig. 4(a), we display the maximum −20 dB comb bandwidth versus the FWHM of $|r_{eff}|^2$. Very narrow bandwidth reflection coefficients, such as 3 GHz, are effective in reducing the comb bandwidth. Further, they are often characterized by a strongly nonlinear phase of the reflection coefficient around ω_0, which tends to favor more irregular, phase unlocked regimes. On the other hand, we can observe a saturation effect in the maximum comb bandwidth for increasing FWHM. This happens because much larger reflectivity bandwidths imply more longitudinal modes above threshold, with larger dispersion and out of the FWM locking range, to reach threshold. This leads to a stronger modal competition, hindering phase locking and, in turn, giving rise to dynamical regimes that are more complex than OFCs. Because of this trade-off, the maximum OFC −20 dB bandwidth that we have been able to observe lies at about 98 GHz, for FWHM = 12 GHz, as illustrated in Fig. 4(a). The overall comb line separation ranges between about 5 and 10 GHz. We remind that such line separation is usually dictated by the separation in frequency of the two CW solutions as in Fig. 1(b).

The result displayed in Fig. 4(a) are in good agreement with experimental evidences, such as [2], where an FWHM of $r_{eff} \approx 3$ GHz resulted in a −50 dB comb bandwidth containing 17 spectral lines, separated about 5.5 GHz from each other. From figures in [2], we can deduce a −20 dB comb bandwidth of about 20 GHz, fairly close to the results reported in Fig. 4(a).

We then aim to address the quality of the resulting OFC, by verifying that the differential phase and amplitude noise of the spectral lines in the generated multimode regimes are extremely small. To perform this characterization, we make use of the quantifiers $\sigma_{\delta\varphi}$ and σ_P, introduced in [17]. In particular, $\sigma_{\delta\varphi}$ is defined as the standard deviation of the differential phase fluctuation between adjacent comb lines and σ_P is the root mean square of the intensity noise of each comb line. We highlight that for an ideal comb we expect such quantifiers to have very small, almost-zero values. In Fig. 4(b), we apply the two quantifiers to the combs identified in Fig. 4(a), isolating all comb

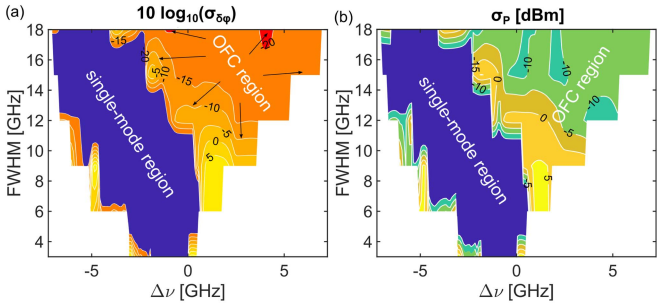

Fig. 5. Maps of the phase (a) and amplitude (b) noise quantifiers as a function of frequency detuning with respect to the effective reflectivity peak (x-axis) and $|r_{eff}|^2$ bandwidth (y-axis). The RSOA bias current is fixed at 300 mA.

lines within the -20 dB bandwidth and calculating the average quantifier values among lines, for different reflectivity FWHMs. As illustrated, the average value of the quantifiers is much lower than the resulting value for more irregular turbulent regimes. Further, focusing on the phase noise quantifier, we record values well below 0.1, similarly to [18], where more irregular regimes are characterized by $\sigma_{\delta\varphi} > 0.1$, attesting the quality of our OFCs.

Finally, in Fig. 5, we map the quantifier values for the whole detuning range $\Delta\nu$ at different reflectivity bandwidths with the aim of identifying more accurately the OFC regions. We highlight that different $|r_{eff}|^2$ FWHMs result in different detuning ranges because of the different associated effective length [9]. In Fig. 5(a), we identify the region of single-mode emission, as the region where, by definition, $\sigma_{\delta\varphi} = 0$. Such a region lies approximately in the negative detuning portion of the map, mainly due to the negative feedback stabilization mechanism associated to the phenomenon of detuned loading [6]. Such single-mode region is excluded from Fig. 5(b), and plotted in blue, to allow for an easier comparison between different multimode regimes. The OFC regime can be easily identified as the orange region in Fig. 5(a), where $10\log_{10}(\sigma_{\delta\varphi}) < -10$. Yellow regions can be instead identified with other multimode phase unlocked regimes. Fig. 5(b) displays the corresponding amplitude noise quantifier values: here, we can approximately associate the OFC region to $\sigma_P < -5$ dBm, in green colors. We also observe that reflectivity bandwidths smaller than 9 GHz display OFCs only in very negatively detuned cases, as the one in Fig. 2. In the case of larger $|r_{eff}|^2$ bandwidths, OFC are more likely to be observed in regions of the parameter space where the phase shift $\Delta\phi$ results in a CW solution of the oscillation condition on the right side of the effective reflectivity peak.

V. Conclusion

We addressed the generation of OFCs in a III-V SiN hybrid laser, identifying the relevant physical mechanisms destabilizing the CW solution and consequently giving rise to OFCs. The resulting combs, displaying both AM and FM modulation, have been characterized in terms of bandwidth, phase and amplitude noise. Future work will consist in the investigation of the impact of nonlinear effects in the SiPh circuit on the OFC regime.

References

[1] L. Chang, S. Liu, and J. E. Bowers, "Integrated optical frequency comb technologies," *Nature Photon.*, vol. 16, no. 2, pp. 95–108, 2022.

[2] J. Mak et al., "Linewidth narrowing via low-loss dielectric waveguide feedback circuits in hybrid integrated frequency comb lasers," *Opt. Exp.*, vol. 27, no. 9, pp. 13307–13318, Apr. 2019. [Online]. Available: https://opg.optica.org/oe/abstract.cfm?URI=oe-27-9-13307

[3] D. Huang et al., "High-power sub-kHz linewidth lasers fully integrated on silicon," *Optica*, vol. 6, no. 6, pp. 745–752, Jun. 2019. [Online]. Available: https://opg.optica.org/optica/abstract.cfm?URI=optica-6-6-745

[4] B. Shen et al., "Integrated turnkey soliton microcombs," *Nature*, vol. 582, no. 7812, pp. 365–369, 2020.

[5] M. Piccardo et al., "Frequency combs induced by phase turbulence," *Nature*, vol. 582, no. 7812, pp. 360–364, 2020, doi: 10.1038/s41586-020-2386-6.

[6] M. A. Tran, D. Huang, and J. E. Bowers, "Tutorial on narrow linewidth tunable semiconductor lasers using Si/III-V heterogeneous integration," *APL Photon.*, vol. 4, no. 11, 2019, Art. no. 111101, doi: 10.1063/1.5124254.

[7] H. M. J. Bastiaens et al., "First demonstration of a hybrid integrated InP-Si3N4 diode laser for broadband optical frequency comb generation," *Proc. SPIE*, vol. 11705, pp. 11–18, 2021, doi: 10.1117/12.2593818.

[8] A. Memon et al., "Using hybrid integrated InP-Si $_3$ N$_4$ diode lasers for the generation of sub-GHz repetition rate frequency combs," *Proc. SPIE*, vol. 12424, pp. 91–99, 2023, doi: 10.1117/12.2661210.

[9] C. Rimoldi, L. L. Columbo, J. Bovington, S. Romero-García, and M. Gioannini, "Damping of relaxation oscillations, photon-photon resonance, and tolerance to external optical feedback of III-V/SiN hybrid lasers with a dispersive narrow band mirror," *Opt. Exp.*, vol. 30, no. 7, pp. 11090–11109, Mar. 2022. [Online]. Available: https://opg.optica.org/oe/abstract.cfm?URI=oe-30-7-11090

[10] E. Detoma, B. Tromborg, and I. Montrosset, "The complex way to laser diode spectra: Example of an external cavity laser strong optical feedback," *IEEE J. Quantum Electron.*, vol. 41, no. 2, pp. 171–182, Feb. 2005.

[11] C. Rimoldi, L. L. Columbo, J. Bovington, S. Romero-García, and M. Gioannini, "CW emission and self-pulsing in a III-V/SiN hybrid laser with narrow band mirror," *IEEE Photon. J.*, vol. 14, no. 4, pp. 1–7, Aug. 2022.

[12] L. Chrostowski and M. Hochberg, *Silicon Photonics Design: From Devices to Systems*. New York, NY, USA: Cambridge Univ. Press, 2015.

[13] L. Columbo, J. Bovington, S. Romero-Garcia, D. F. Siriani, and M. Gioannini, "Efficient and optical feedback tolerant hybrid laser design for silicon photonics applications," *IEEE J. Sel. Topics Quantum Electron.*, vol. 26, no. 2, pp. 1–10, Mar./Apr. 2020.

[14] B. Tromborg, J. Mørk, and V. Velichansky, "On mode coupling and low-frequency fluctuations in external-cavity laser diodes," *Quantum Semiclassical Opt.: J. Eur. Opt. Soc. Part B*, vol. 9, no. 5, Oct. 1997, Art. no. 831, doi: 10.1088/1355-5111/9/5/014.

[15] P. Bardella and I. Montrosset, "Analysis of self-pulsating three-section DBR lasers," *IEEE J. Sel. Topics Quantum Electron.*, vol. 11, no. 2, pp. 361–366, Mar./Apr. 2005.

[16] L. L. Columbo, J. Bovington, D. Siriani, S. Romero-García, and M. Gioannini, "Time domain traveling wave model of optical feedback tolerant hybrid laser design for silicon photonics applications (Conference Presentation)," *Proc. SPIE*, vol. 11301, 2020, Art. no. 113010G, doi: 10.1117/12.2546731.

[17] P. Bardella, L. L. Columbo, and M. Gioannini, "Self-generation of optical frequency comb in single section quantum dot fabry-perot lasers: A theoretical study," *Opt. Exp.*, vol. 25, no. 21, pp. 26234–26252, Oct. 2017. [Online]. Available: https://opg.optica.org/oe/abstract.cfm?URI=oe-25-21-26234

[18] C. Silvestri, L. L. Columbo, M. Brambilla, and M. Gioannini, "Coherent multi-mode dynamics in a quantum cascade laser: Amplitude- and frequency-modulated optical frequency combs," *Opt. Exp.*, vol. 28, no. 16, pp. 23846–23861, Aug. 2020. [Online]. Available: https://opg.optica.org/oe/abstract.cfm?URI=oe-28-16-23846

Open Access funding provided by 'Politecnico di Torino' within the CRUI CARE Agreement